frontiers | Frontiers in Physics

TYPE Brief Research Report
PUBLISHED 10 October 2024
DOI 10.3389/fphy.2024.1475071

OPEN ACCESS

EDITED BY
Chong Zu,
Washington University in St. Louis, United States

REVIEWED BY
Wengang Zhang,
Beijing academy of quantum information science, China
De-Sheng Li,
Hunan Institute of Engineering, China

*CORRESPONDENCE
Hamidreza Siampour,
h.siampour@qub.ac.uk

RECEIVED 02 August 2024
ACCEPTED 25 September 2024
PUBLISHED 10 October 2024

CITATION
Snow K, Moradiani F and Siampour H (2024) Strip-loaded nanophotonic interfaces for resonant coupling and single-photon routing. *Front. Phys.* 12:1475071.
doi: 10.3389/fphy.2024.1475071

Strip-loaded nanophotonic interfaces for resonant coupling and single-photon routing

Katharine Snow, Fatemeh Moradiani and Hamidreza Siampour*

School of Mathematics and Physics, Queen's University Belfast, University Road, Belfast, United Kingdom

We report on the design and simulation of strip-loaded nanophotonic interfaces aimed at improving resonant coupling and photon routing efficiency. In our design, the guided mode is confined within a plane by a high-index thin film and is loosely confined laterally by a lower index strip. Using a hydrogen silsesquioxane (HSQ) strip, titanium dioxide core, and silicon dioxide substrate, we optimise the waveguide dimensions for maximum lateral confinement of light. Specifically, we propose a polymer-based Bragg grating cavity and ring resonator that achieve near-optimal mode volumes and high Q-factors. These may be further developed to achieve the even higher Q-factors demanded by quantum technologies. Our calculations suggest that a quantum dot embedded in a cavity with a mode volume of $V_{eff} \sim 7.0\,(\lambda/n)^3$ and a Q-factor of 7,000 can produce photons with 97% indistinguishability at 4K. Additionally, we investigate directional couplers for efficient photon routing, comparing photonic and plasmonic material structures. While pure photonic structures demonstrate lower loss and improved quality factors, they face practical limitations in terms of bending radius. Conversely, plasmonic structures offer shorter bending radii but higher propagation losses. This research lays the groundwork for future nanophotonic designs, aiming to enhance photon generation and routing capabilities for quantum optical applications.

KEYWORDS

nanophotonics and photonic crystals, quantum, spin qubit, solid-state, optics and photonics

Introduction

Quantum emitters of single indistinguishable photons are critical for advancing quantum technologies such as computing [1], networking [2], cryptography [3], and metrology [4]. Currently, spontaneous parametric down-conversion is the prevalent method for single-photon generation, but its probabilistic nature limits how far the efficiency and indistinguishability of photons can be simultaneously increased [5]. Solid-state emitters, including semiconductor quantum dots [6, 7] and diamond colour centres [8, 9], offer promising alternatives that are not subject to the same constraints when integrated with nanophotonic devices. By placing the emitters inside a high-Q cavity, the emitter's decay rate is enhanced by the Purcell factor F_P, which reduces the effects of dephasing and decay to unwanted modes. Unlike placing the emitter in a waveguide, using a cavity also filters out the non-Markovian phonon sideband without sacrificing efficiency [10]. This is crucial when using emitters with a large sideband, as achieving near-unity efficiency is a primary research focus due to the stringent requirements imposed by all potential applications.

To achieve narrowband enhancement of the zero-phonon line (ZPL), the cavity decay rate κ must satisfy the condition $\kappa \ll \xi$ where ξ is the typical energy scale of coupled phonons. The single figure of merit is the Purcell factor, which is engineered to be as high as possible, subject to the constraint of weak coupling. The Purcell factor is given by Equation 1:

$$F_P = \frac{2g^2}{\Gamma\kappa} = \frac{3}{4\pi^2}\frac{Q}{V_{eff}/(\lambda/n)^3} \quad (1)$$

where g is the emitter-cavity coupling rate, Γ is the emitter's vacuum decay rate, κ is the cavity decay rate, Q is the cavity quality factor, and V_{eff} is its mode volume. Increasing the Purcell factor therefore means increasing the coupling g while keeping κ just within the limit of weak coupling, $\kappa/2 \geq g$. In more practical terms, this equates to reducing the mode volume as far as possible and increasing Q to just within the weak coupling limit. The coupling cannot be increased arbitrarily, however, without losing the narrowband enhancement, $\kappa \ll \xi$. There has been a focus on designing cavities with deeply sub-wavelength mode volumes, which are theoretically achievable using slot waveguides or plasmonic devices [11–13], through both direct and inverse design approaches [14–16]. However, experimentally, the best-performing devices use quantum dots embedded in conventional Bragg cavities, with mode volumes on the order of $V_{eff} \sim (\lambda/2n)^3$, and lossy plasmonic components are avoided. Quantum dots in micropillar cavities at cryogenic temperatures have been used to generate single photons with indistinguish abilities greater than 0.99 and efficiencies around 0.9—excluding inefficiencies in out-coupling or initial excitation—which has enabled their use in generating small photonic cluster states of approximately 10 qubits [17, 18].

Micropillar cavities are chosen for their high Q-factors upon fabrication. The difficulty of precise nanoscale positioning of the emitter within the cavity also prohibits the use of ultra-small mode volumes. The second reason for avoiding ultra-small mode volumes is that the narrowband enhancement is lost. Under the constraints $\kappa/2 \geq g$ and $\kappa \ll \xi$, there is a maximum Purcell enhancement of $F_P\Gamma \sim \xi/20$ for the optimal values $\kappa \sim \xi/10$ and $g \sim \xi/20$. For quantum dots with $\xi \sim$1.45me, we demonstrate that this corresponds to $Q \sim$7,000, $V_{eff} \sim 7.0(\lambda/n)^3$, and $F_P \sim$50.

Here, we propose a polymer-based Bragg grating cavity and ring resonator. Such polymer-based nanophotonic devices can be fabricated with very high precision using current fabrication technology [9, 19]. Due to the low refractive index of hydrogen silsesquioxane (HSQ) polymer, we choose a strip-loaded waveguide geometry, which results in a larger mode volume than current devices, with $V_{eff} \sim 7.0(\lambda/n)^3$. When interfaced with a quantum dot at 4K, we predict that a cavity with this mode volume, if further developed and accurately fabricated to give $Q \sim$7,000, will generate photons with an indistinguishability of 97% and an efficiency of 98%. Our cavity provides a model on which further design improvements may be built, to achieve the necessary very high Q-factors and low footprint in these devices, within the planar configuration that makes them suitable for on-chip manipulation of the emitted photons.

Results and discussion

Bragg grating cavity

In a strip-loaded waveguide, the mode is confined within a plane by a high-index thin film and is loosely confined in the lateral direction by a lower index strip, as shown in Figure 1Ai. We choose an HSQ strip, titanium dioxide core, and silicon dioxide substrate, and optimise the waveguide dimensions for maximum lateral confinement of light with a vacuum wavelength of approximately 600 nm. The optimal dimensions are as follows: strip height of 180 nm, strip width of 300 nm, and core thickness of 70 nm. A Bragg cavity is constructed based on this waveguide geometry, with the Bragg reflectors being twice as long as the waveguide is wide, as shown in the inset of Figure 1Aii. The transmission spectrum of this cavity is shown in Figure 1Aii for different values of the total number of Bragg reflectors N. For N = 100, the quality factor is found to be 230 and the outcoupling efficiency, defined as the cavity-waveguide coupling ratio, is 90%. The cavity mode is shown in Figure 1C, and the mode volume is found to be 6.96 $(\lambda/n)^3$. We also show the stopband in Figure 1Aiii and, for comparison, in Figure 1B the equivalent results for a plasmonic cavity with the same HSQ strip [20].

The quantum emitter should be embedded in the cavity at the position where the cavity mode electric field is maximal. Emitted photons need to have both high indistinguishability, defined as the ability of two photons to interfere on a beam-splitter in a Hong-Ou-Mandel setup, and high quantum efficiency, defined as the fraction of photons emitted into the cavity. In the narrowband-enhancement weak-coupling regime (see Figure 2), the indistinguishability and efficiency of emitted photons are given by $= \frac{F_P+1}{F_P+1+\frac{2\gamma}{\Gamma}}$, and $\eta = \frac{B^2F_P}{B^2F_P+1}$, respectively, where γ is the dephasing rate and B, known as the Frank-Condon factor, is the square-root probability of photon emission into ZPL [10]. For example, for a quantum dot at 4K the optimal values of Q and V_{eff} — corresponding to $\kappa \sim \xi/10$ and $g \sim \xi/20$—are given by $Q = \frac{\omega}{2\kappa}$, and $V_{\text{eff}} = \frac{\omega\mu^2}{2\hbar\epsilon_0 n^2 g^2}$, where ω is the angular frequency and μ the dipole moment. Taking $\mu = 27.2D$ [21], $2\pi c\omega$ = 600 nm and ξ = 1.45 meV, we find the optimal values Q = 7,100 and $V_{\text{eff}} = 7\ (\lambda/n)^3$. We should note that the wavelength used in these calculations is that of our proposed cavity, which differs from that of typical QDs by a factor of 1.5.

To determine the indistinguishability, we follow ref. [10]: we assume that the dominant contribution to the dephasing γ is due to phonons. This assumption holds in electrically contacted structures, where charge and spin noise are minimized [22]. We also assume a bulk phonon spectrum, achievable through clamping [23]. The dephasing then depends on g and κ through Equation 2:

$$\gamma = 2\pi\left(\frac{gB}{\kappa}\right)^2 J(2gB)\coth\left(\frac{\hbar gB}{k_BT}\right) \quad (2)$$

where $J(\nu) = \alpha\nu^3\exp(-(\frac{\nu}{\xi})^2)$, $\alpha = 0.03ps^2$ is the exciton–phonon coupling strength, T is the temperature, and we take B = 0.95 [10]. In Figure 2, we show the combined value $I\eta$ as a function of V_{eff} and Q. The regions outside the narrowband-enhancement weak-coupling regime have been excluded. At the point where F_P is at its maximum, the indistinguishability is I = 0.97 and the efficiency is η = 0.98.

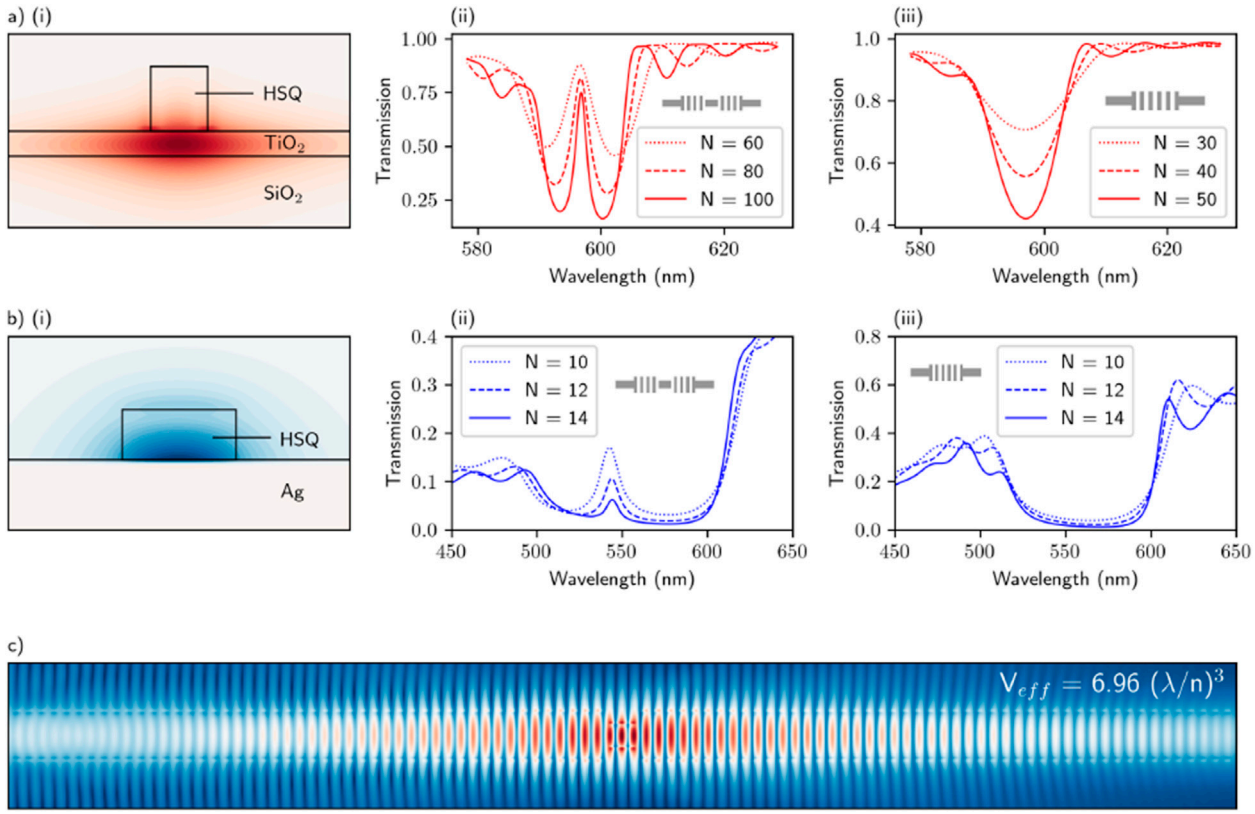

FIGURE 1
Electromagnetic simulations of polymer-based nanophotonic devices. **(A)** A strip-loaded waveguide and **(B)** a plasmonic waveguide. Cross-sections of the modes are depicted in (i). Transmission spectra for the corresponding Bragg cavities and Bragg reflectors are presented in (ii) and (iii), respectively, for various values of N, the number of reflectors. The strip-loaded cavity mode for N = 100 is shown in **(C)**.

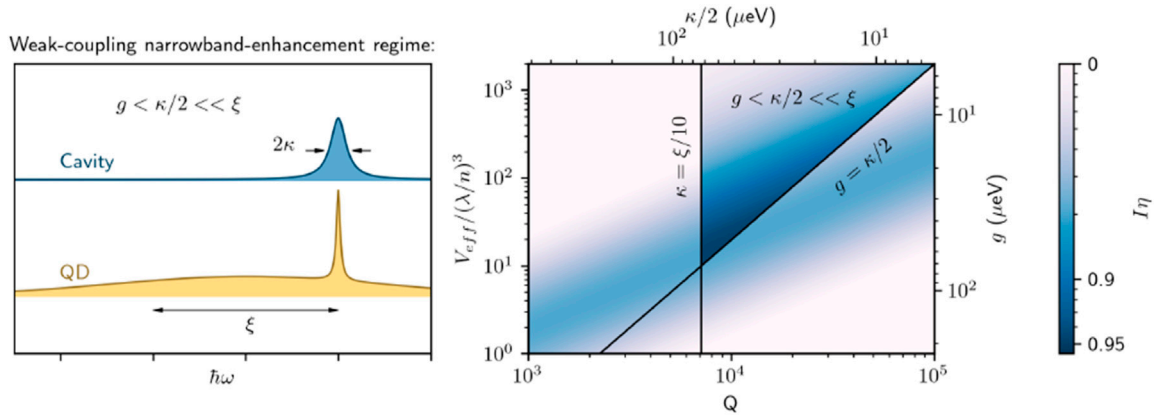

FIGURE 2
The narrowband-enhancement weak-coupling regime for a quantum dot embedded in a nanophotonic cavity. Left: A sketch illustrating the different energy scales of importance, where the cavity linewidth is much smaller than the typical energy scale of phonons. Right: The product $I\eta$ of the indistinguishability I and the efficiency η must be close to 1 for optimal quantum photonic applications. This product is plotted as a function of the Q-factor and mode volume. In our calculation, we follow ref. [10]: we assume that dephasing is primarily due to phonon effects and use typical experimental values for the coupling parameters in quantum dots.

10.3389/fphy.2024.1475071

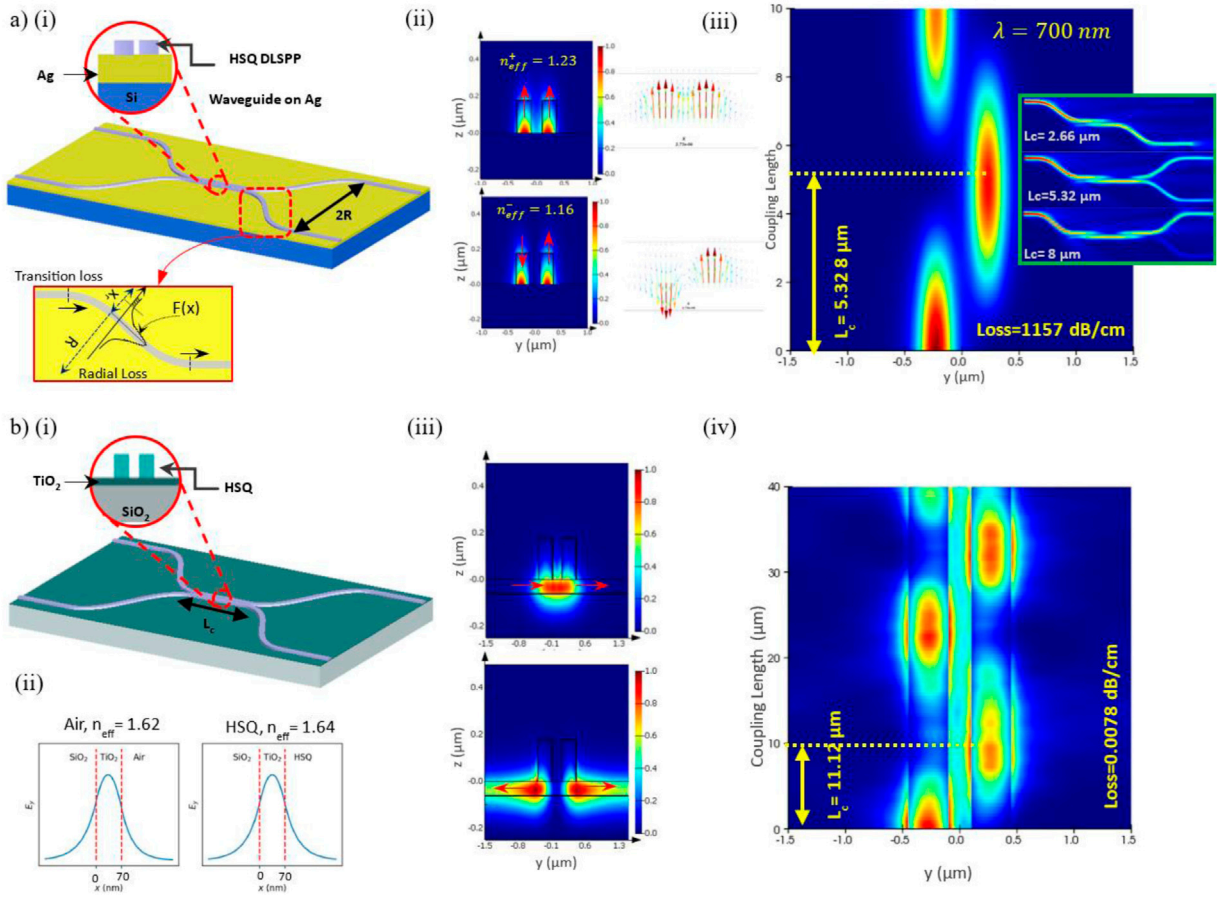

FIGURE 3
(A) Simulation results of a DLSPP-based directional coupler structure consisting of two rectangular DLSPP waveguides with a height of h = 180 nm, width of w = 250 nm, refractive index n_d = 1.41, a separation gap of g = 200 nm in the parallel section, and an S-bend waveguide with a 2.5 μm radius. The length of the parallel section (coupling length) is Lc = 5.3 μm, designed to impart a π phase shift and achieve 50–50 power splitting at λ = 700 nm between the (ii) symmetric (n^{+}_{eff}) and (iii) anti-symmetric (n^{-}_{eff}) DLSPP modes supported by (iv) the structure using $L_c = \lambda/2\,(n^{+}_{eff} - n^{-}_{eff})$. The surface shows the electric field norm (V/m) profile with red arrows indicating the E-field. Insets (ii): E-field mode vectors for symmetric and anti-symmetric modes. Inset (iv): The full profile of DLSPP directional couplers with a 200 nm gap and radii of 2.66, 5.32, and 8 μm, achieving 0–100, 50–50, and 100–0 power coupling, respectively. **(B)** Simulation results of the strip-loaded directional coupler structure consisting of two rectangular strip-loaded waveguides with a height of h = 180 nm, width of w = 250 nm, refractive index n_d = 1.41, a separation gap of g = 200 nm in the parallel section, and an S-bend waveguide with a 100 μm radius on a TiO_2 layer with a height of 70 nm. The length of the parallel section (coupling length) is L_c = 11.2.

Directional coupler

The concept of the directional coupler, introduced in the mid-20th century, has been foundational for many advancements in optical and microwave technologies [24]. While the fundamental idea remains relevant, the design of the entire structure—including S-bends and a chain of materials tailored for specific applications—continues to hold significant importance in contemporary engineering. More recently, the directional coupler has become a crucial component in photonic quantum integrated circuits, demonstrating the capability to facilitate quantum computing logic operations when employed with single photons [25–27].

In this section, we present two platforms for directional couplers: one based on dielectric-loaded surface plasmon polariton (DLSPP) waveguides and the other on strip-loaded waveguide configurations. We then compare the two structures in terms of their applicability for single-photon routing. Notably, the overall dimensions of both platforms are consistent with the Bragg grating cavity structure discussed in the previous section.

The directional coupler is designed for both parallel straight waveguides and S-bends based on sine curves, enabling continuous bend curvature and adiabatic modification [28–30] of the DLSPP waveguide and the strip-loaded waveguide mode throughout the bend, as shown in Figures 3Ai, Bi, respectively. One crucial aspect to consider is the design of the S-bend. As illustrated in Figure 3A, the losses associated with the S-bend can be categorised into transition losses and radial losses.

Radial losses occur due to the limited guiding of the propagation mode caused by speed limitations beyond the outer end of the bent waveguide. Transition losses occur when there are discontinuities in the curvature of the waveguide, where sudden changes in modal propagation characteristics take place. The guided modes in curved waveguides are broader compared to straight waveguides and change outward along the curve. The normalised transition loss

due to mismatch between the straight waveguide mode and the curvature can be calculated as follows in Equation 3 [29].

$$\Gamma_T = 1 - \frac{\left|\iint E_{in}(x,y)E^{*}_{out}(x,y)dydx\right|^2}{\iint\left|E_{in}(x,y)\right|^2\iint\left|E_{out}(x,y)\right|^2 dxdy} \quad (3)$$

where E_{in} and E_{out} represent the electrical input and output mode fields, respectively. The normalised radial loss, related to the radial attenuation coefficient $\alpha(R,l)$ per unit length l in a bend radius R, can be expressed as [29]: $\Gamma_R = exp(-\int_L^o \alpha(R(l'),l')dl')$.

In this study, we utilised the commercial software Lumerical FDTD to calculate the minimum bending radius R_{min}. The design of the S-bends was based on sine curves [31, 32], allowing for continuous bend curvature and thereby adiabatic modification of the mode throughout the bend. For the DLSPP structure, due to its high optical contrast and strong confinement of the DLSPP mode, a curvature radius as small as 2 μm still transmitted a significant portion of the DLSPP mode (>50%). This finding is consistent with experimental measurements using scanning near-field optical microscopy (SNOM) [31].

For the strip-loaded structure, where the effective mode index with HSQ cladding differs from that with air by a small amount of 0.02 (from 1.64 to 1.62, as shown in Figure 3Bii), the minimum bending radius must be sufficiently large to allow the light to bend effectively. We calculated this value from simulations to be 100 μm [33], which is close to the value obtained from the analytical expression in reference [34]. From this expression, $R_{min} \approx 0.1325\lambda_0/[(n_1 - n_2)/n_1]^{3/2}$, we estimated the minimum bending radius to be approximately 70 μm, where n_1 and n_2 are the effective indices with and without HSQ cladding, respectively."

This characteristic is crucial for designing optical devices with tight bends and for sensitive optical applications, such as single-photon routing. However, in applications like single-photon sources, the overall propagation length is limited by structural and environmental factors when the emitter is coupled to the waveguide. Although the photon propagation length is generally longer than that of SPPs, issues may arise concerning the structure's overall length. Additionally, in these structures, distinguishability may be significantly compromised at very high dimensions. Nevertheless, the strip-loaded structure remains a strong option for applications where minimising loss is the primary concern.

The interaction length required to achieve the desired power coupling to the second waveguide is calculated using $L_c = \lambda/2(n^+_{eff} - n^-_{eff})(\sin^{-1}(\sqrt{P_{out2}/P_{in}}))$. For a π phase shift, the relation simplifies $L_c = \lambda/2(n^+_{eff} - n^-_{eff})$ [35, 36]. Figure 3Aiii and Figure 3Biv show the numerical calculations of the coupling length for both DLSPP and strip-loaded structures, using symmetric (Figure 3Aii top and Figure 3Biii top) and asymmetric modes (Figure 3Aii bottom and Figure 3Biii bottom) at a wavelength of 700 nm. While strip-loaded structures generally exhibit lower loss compared to DLSPP structures, their large radius of curvature can still limit their practical application in certain scenarios.

Ring resonator

Another approach to enhancing the Purcell effect is to use DLSPP waveguide-ring resonators (WRRs). A WRR, consisting of a straight waveguide laterally coupled to a ring resonator, typically provides more pronounced wavelength selection and a high Q-factor, which is crucial in integrated optics. It is important to note that the extinction ratio, which indicates the contrast in transmission through a WRR between resonant and non-resonant wavelengths, is affected by both the coupling efficiency and the internal loss within the resonator [37]. In plasmonic WRRs, coupling efficiency is usually low due to the tight confinement in plasmonic waveguides, while internal loss is high due to propagation loss. As a result, achieving critical coupling for a high extinction ratio can be challenging.

Figure 4A shows a 3D schematic of the DLSSP-WRR structure, designed with the same parameters discussed in the previous section. Figure 4B presents the transmission spectrum for a ring with a radius of 2.5 μm and three different separations (g) of 200 nm, 150 nm, and 100 nm. A 100 nm gap provides a higher extinction ratio compared to the other gaps, though this enhanced coupling efficiency also leads to mode broadening. Figure 4C depicts the full profile of the structure at a resonant wavelength of 616.4 nm and a non-resonant wavelength of 623 nm. The bandwidth of the WRR is determined by the radius of the ring resonator and the wavelength-dependent effective index of the bent waveguide. Figure 4D displays the transmission spectra for a 100 nm separation and ring radii ranging from 2 μm to 3.5 μm in 0.5 μm increments. Increasing the ring radius improves the maximum resolution of the DLSSP, resulting in a higher quality factor. Figure 4E shows the mode area of the 250 nm width HSQ as a function of HSQ thickness (h). The mode area definition related to the Purcell effect, based on [10], indicates that as HSQ thickness increases from 160 nm to 240 nm, the effective mode area remains unchanged. However, for h < 160 nm, mode leakage into the air cladding increases the mode area. Additionally, we have computed the mode area, normalized Purcell factor, and quality factor of the structure for various ring radii. As the ring radius increases, the bandwidth decreases, leading to an increase in the quality factor. For a ring with a radius of 2.5 μm, the Purcell factor and quality factor are ~10 and ~133, respectively, which are relatively high compared to a strip-loaded waveguide.

Conclusion

We have introduced the design and simulation of a polymer-based Bragg grating cavity with a strip-loaded waveguide. The optimal parameters for this design include a mode volume of $V_{eff} \sim 7.0(\lambda/n)^3$, with predicted photon indistinguishability of 97% and efficiency of 98% for a cavity with a Q-factor of approximately 7,000. Our analysis compared two types of directional couplers: DLSPP and strip-loaded waveguides, evaluating their design, performance, and limitations, with a focus on their applicability for single-photon routing. Additionally, we explored ring resonators for enhancing the Purcell effect, presenting simulations of a DLSSP-based ring resonator with various parameters. The results showed that increasing the ring radius improves resolution and quality factor but may lead to broader mode profiles. Our findings suggest that polymer-based cavities, specifically using HSQ, can achieve high

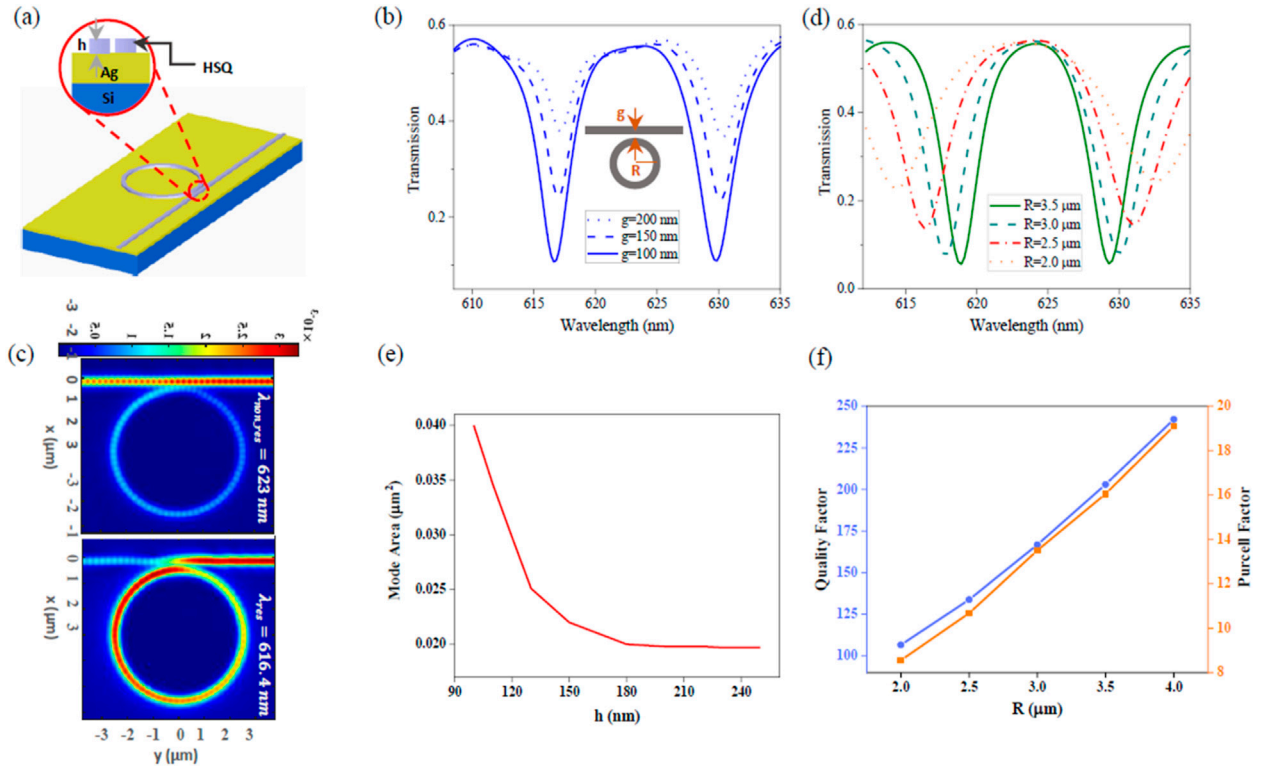

FIGURE 4
(A) Sketch of the DLSSP-WRR. **(B)** Transmission spectrum of the HSQ DLSPP-loaded ring-resonator cavity with a 2.5 μm radius, showing spectra for separation gaps of 200 nm, 150 nm, and 100 nm. **(C)** Full profile of the structure at the resonant wavelength of 616.4 nm and the non-resonant wavelength of 623 nm, for a separation gap of 100 nm. **(D)** Mode area as a function of HSQ thickness. **(E)** Calculated mode area as a function of HSQ thickness. **(F)** Quality factor and Purcell factor as functions of ring radius. In the transmission spectra **(B)**, different ring radii (2.0, 2.5, 3.0, and 3.5 μm) are displayed. The wavelength range from 610 nm to 635 nm is plotted to highlight the transmission characteristics at various separations and ring radii.

Q-factors and significant Purcell factors. These structures are promising for practical quantum photonics applications due to their planar configuration, which facilitates on-chip integration. The proposed structures, including Bragg gratings and ring resonators, have demonstrated high potential for improving photon indistinguishability and efficiency, which are crucial for advancing quantum technologies.

Data availability statement

The raw data supporting the conclusions of this article will be made available by the authors, without undue reservation.

Author contributions

KS: Formal Analysis, Investigation, Methodology, Software, Writing–original draft, Writing–review and editing. FM: Formal Analysis, Investigation, Methodology, Software, Writing–original draft, Writing–review and editing. HS: Conceptualization, Formal Analysis, Funding acquisition, Investigation, Resources, Software, Supervision, Validation, Visualization, Writing–original draft, Writing–review and editing.

Funding

The author(s) declare that financial support was received for the research, authorship, and/or publication of this article. This work was funded by the UKRI Strength in Places Fund programme Smart Nano NI, and the Engineering and Physical Sciences Research Council (EPSRC) under grant number EP/S023321/1.

Conflict of interest

The authors declare that the research was conducted in the absence of any commercial or financial relationships that could be construed as a potential conflict of interest.

Publisher's note

All claims expressed in this article are solely those of the authors and do not necessarily represent those of their affiliated organizations, or those of the publisher, the editors and the reviewers. Any product that may be evaluated in this article, or claim that may be made by its manufacturer, is not guaranteed or endorsed by the publisher.

References

1. Briegel HJ, Browne DE, Dür W, Raussendorf R, Van den Nest M. Measurement-based quantum computation. *Nat Phys* (2009) 5:19–26. doi:10.1038/nphys1157

2. Azuma K, Tamaki K, Lo H-K. All-photonic quantum repeaters. *Nat Commun* (2015) 6:6787. doi:10.1038/ncomms7787

3. Kołodyński J, Máttar A, Skrzypczyk P, Woodhead E, Cavalcanti D, Banaszek K, et al. Device-independent quantum key distribution with single-photon sources. (2018) doi:10.48550/arXiv.1803.07089

4. Giovannetti V, Lloyd S, Maccone L. Advances in quantum metrology. *Nat Photon* (2011) 5:222–9. doi:10.1038/nphoton.2011.35

5. Meyer-Scott E, Silberhorn C, Migdall A. Single-photon sources: approaching the ideal through multiplexing. *Rev Scientific Instr* (2020) 91:041101. doi:10.1063/5.0003320

6. Somaschi N, Giesz V, De Santis L, Loredo JC, Almeida MP, Hornecker G, et al. Near-optimal single-photon sources in the solid state. *Nat Photon* (2016) 10:340–5. doi:10.1038/nphoton.2016.23

7. Siampour H, O'Rourke C, Brash AJ, Makhonin MN, Dost R, Hallett DJ, et al. Observation of large spontaneous emission rate enhancement of quantum dots in a broken-symmetry slow-light waveguide. *npj Quan Inf* (2023) 9:15. doi:10.1038/s41534-023-00686-9

8. Shandilya PK, Flagan S, Carvalho NC, Zohari E, Kavatamane VK, Losby JE, et al. Diamond integrated quantum nanophotonics: spins, photons and phonons. *J Lightwave Technol* (2022) 40:7538–71. doi:10.1109/jlt.2022.3210466

9. Siampour H, Kumar S, Davydov VA, Kulikova LF, Agafonov VN, Bozhevolnyi SI. On-chip excitation of single germanium vacancies in nanodiamonds embedded in plasmonic waveguides. *Light: Sci and Appl* (2018) 7:61. doi:10.1038/s41377-018-0062-5

10. Iles-Smith J, McCutcheon DPS, Nazir A, Mørk J. Phonon scattering inhibits simultaneous near-unity efficiency and indistinguishability in semiconductor single-photon sources. *Nat Photon* (2017) 11:521–6. doi:10.1038/nphoton.2017.101

11. Hu S, Weiss SM. Design of photonic crystal cavities for extreme light concentration. *ACS Photon* (2016) 3:1647–53. doi:10.1021/acsphotonics.6b00219

12. Siampour H, Dan Y. Si nanowire phototransistors at telecommunication wavelengths by plasmon-enhanced two-photon absorption. *Opt Express* (2016) 24:4601–9. doi:10.1364/oe.24.004601

13. Guimbao J, Sanchis L, Weituschat L, Manuel Llorens J, Song M, Cardenas J, et al. Numerical optimization of a nanophotonic cavity by machine learning for near-unity photon indistinguishability at room temperature. *ACS Photon* (2022) 9:1926–35. doi:10.1021/acsphotonics.1c01651

14. Malkiel I, Mrejen M, Nagler A, Arieli U, Wolf L, Suchowski H. Plasmonic nanostructure design and characterization via Deep Learning. *Light: Sci and Appl* (2018) 7:60. doi:10.1038/s41377-018-0060-7

15. Piggott AY, Lu J, Lagoudakis KG, Petykiewicz J, Babinec TM, Vučković J. Inverse design and demonstration of a compact and broadband on-chip wavelength demultiplexer. *Nat Photon* (2015) 9:374–7. doi:10.1038/nphoton.2015.69

16. Siampour H, Nezhad AZ. Revealing the invisible: imaging through non-radiating subspace. *J Opt Photon Res* (2024). doi:10.47852/bonviewjopr42022785

17. Coste N, Fioretto DA, Belabas N, Wein SC, Hilaire P, Frantzeskakis R, et al. High-rate entanglement between a semiconductor spin and indistinguishable photons. *Nat Photon* (2023) 17:582–7. doi:10.1038/s41566-023-01186-0

18. Cogan D, Su Z-E, Kenneth O, Gershoni D. Deterministic generation of indistinguishable photons in a cluster state. *Nat Photon* (2023) 17:324–9. doi:10.1038/s41566-022-01152-2

19. Siampour H, Wang O, Zenin VA, Boroviks S, Siyushev P, Yang Y, et al. Ultrabright single-photon emission from germanium-vacancy zero-phonon lines: deterministic emitter-waveguide interfacing at plasmonic hot spots. *Nanophotonics* (2020) 9:953–62. doi:10.1515/nanoph-2020-0036

20. Siampour H, Kumar S, Bozhevolnyi SI. Chip-integrated plasmonic cavity-enhanced single nitrogen-vacancy center emission. *Nanoscale* (2017) 9:17902–8. doi:10.1039/c7nr05675c

21. Liu F, Brash AJ, O'Hara J, Martins LMPP, Phillips CL, Coles RJ, et al. High Purcell factor generation of indistinguishable on-chip single photons. *Nat Nanotechnology* (2018) 13:835–40. doi:10.1038/s41565-018-0188-x

22. Löbl MC, Söllner I, Javadi A, Pregnolato T, Schott R, Midolo L, et al. Narrow optical linewidths and spin pumping on charge-tunable close-to-surface self-assembled quantum dots in an ultrathin diode. *Phys Rev B* (2017) 96:165440. doi:10.1103/physrevb.96.165440

23. Dreeßen CL, Oullet-Plamondon C, Tighineanu P, Zhou X, Midolo L, Sørensen AS, et al. Suppressing phonon decoherence of high performance single-photon sources in nanophotonic waveguides. *Quan Sci Technology* (2019) 4:015003. doi:10.1088/2058-9565/aadbb8

24. Riblet HJ. A mathematical theory of directional couplers. *Proc IRE* (1947) 35:1307–13. doi:10.1109/jrproc.1947.233573

25. Siampour H, Kumar S, Bozhevolnyi SI. Nanofabrication of plasmonic circuits containing single photon sources. *ACS Photon* (2017) 4:1879–84. doi:10.1021/acsphotonics.7b00374

26. Mrejen M, Suchowski H, Hatakeyama T, Wang Y, Zhang X. Experimental realization of two decoupled directional couplers in a subwavelength packing by adiabatic elimination. *Nano Lett* (2015) 15:7383–7. doi:10.1021/acs.nanolett.5b02790

27. Peruzzo A, Shadbolt P, Brunner N, Popescu S, O'Brien JL. A quantum delayed-choice experiment. *Science* (2012) 338:634–7. doi:10.1126/science.1226719

28. Takagi A, Jinguji K, Kawachi M. Wavelength characteristics of (2*2) optical channel-type directional couplers with symmetric or nonsymmetric coupling structures. *J Lightwave Technol* (1992) 10:735–46. doi:10.1109/50.143072

29. Kruse KL, Middlebrook CT. Fan-out routing and optical splitting techniques for compact optical interconnects using single-mode polymer waveguides. *J Mod Opt* (2015) 62:S1–S10. doi:10.1080/09500340.2014.983197

30. Miyatake Y, Toprasertpong K, Takagi S, Takenaka M. Design of compact and low-loss S-bends by CMA-ES. *Opt Express* (2023) 31:43850–63. doi:10.1364/oe.504866

31. Holmgaard T, Chen Z, Bozhevolnyi SI, Markey L, Dereux A, Krasavin AV, et al. Bend- and splitting loss of dielectric-loaded surface plasmon-polariton waveguides. *Opt Express* (2008) 16:13585–92. doi:10.1364/oe.16.013585

32. Kumar A, Aditya S. Performance of S-bends for integrated-optic waveguides. *Microwave Opt Technology Lett* (1998) 19:289–92. doi:10.1002/(sici)1098-2760(199811)19:4<289::aid-mop13>3.0.co;2-y

33. Doughan I, Oyemakinwa K, Ovaskainen O, Roussey M. Strip-loaded Mach–Zehnder interferometer for absolute refractive index sensing. *Scientific Rep* (2024) 14:3064. doi:10.1038/s41598-024-53326-3

34. Heiblum M, Harris J. Analysis of curved optical waveguides by conformal transformation. *IEEE J Quan Electronics* (1975) 11:75–83. doi:10.1109/jqe.1975.1068563

35. Holmgaard T, Chen Z, Bozhevolnyi SI, Markey L, Dereux A. Design and characterization of dielectric-loaded plasmonic directional couplers. *J Lightwave Technol* (2009) 27:5521–8. doi:10.1109/JLT.2009.2031654

36. Chen Z, Holmgaard T, Bozhevolnyi SI, Krasavin AV, Zayats AV, Markey L, et al. Wavelength-selective directional coupling with dielectric-loaded plasmonic waveguides. *Opt Lett* (2009) 34:310–2. doi:10.1364/ol.34.000310

37. Su Y, Chang P, Lin C, Helmy AS. Record Purcell factors in ultracompact hybrid plasmonic ring resonators. *Sci Adv* (2019) 5:eaav1790. doi:10.1126/sciadv.aav1790